Water vapor diffusive transport in a smectite clay:
Cationic control of normal versus anomalous diffusion

Leander Michels,[1] Yves Méheust,[2,*] Mario A. S. Altoé,[3,4] Éverton C. dos Santos,[1,5] Henrik Hemmen,[1] Roosevelt Droppa Jr.,[6]
Jon O. Fossum,[1,†] and Geraldo J. da Silva[3,‡]

[1]*Department of Physics, NTNU–Norwegian University of Science and Technology, NO-7495 Trondheim, Norway*
[2]*Géosciences Rennes, UMR 6118, Univ. Rennes, CNRS, 35000 Rennes, France*
[3]*Instituto de Física, UnB–Universidade de Brasília, 70.919-970 Brasília DF, Brazil*
[4]*Departamento de Química e Física, UFES–Universidade Federal do Espírito Santo, Alto Universitário,*
S/N, Guararema, 29500-000 Alegre-ES, Brazil
[5]*NBI–Niels Bohr Institute, University of Copenhagen, 2100 Copenhagen, Denmark*
[6]*Centro de Ciências Naturais e Humanas, UFABC–Universidade Federal do ABC, 09.210-580, Santo André SP, Brazil*

The transport of chemical species in porous media is ubiquitous in subsurface processes, including contaminant transport, soil drying, and soil remediation. We study vapor transport in a multiscale porosity material, a smectite clay, in which water molecules travel in mesopores and macropores between the clay grains but can also intercalate inside the nanoporous grains, making them swell. The intercalation dynamics is known to be controlled by the type of cation that is present in the nanopores; in this case exchanging the cations from Na^+ to Li^+ accelerates the dynamics. By inferring spatial profiles of mesoporous humidity from a space-resolved measurement of grain swelling, and analyzing them with a fractional diffusion equation, we show that exchanging the cations changes mesoporous transport from Fickian to markedly subdiffusive. This results both from modifying the exchange dynamics between the mesoporous and nanoporous phases, and from the feedback of transport on the medium's permeability due to grain swelling. An important practical implication is a large difference in the time needed for vapor to permeate a given length of the clay depending on the type of intercalated cation.

I. INTRODUCTION

The transport of chemical species and small molecules in porous media, either as gas or in liquid phase as solutes, plays an important role in a number of environmental processes including contaminant transport, soil drying, and in many industrial subsurface applications, such as soil and aquifer remediation, nuclear waste disposal, or steam EOR (enhanced oil recovery). In this context the conventional description of transport is an extension of the advection-diffusion equation based on Fick's laws, where the molecular coefficient (or diffusivity) is replaced by a much larger dispersion coefficient that accounts for the combined effect of molecular diffusion and heterogeneous advection below the continuum scale [1]. This theoretical framework, in which the spatial variance of transported plumes varies linearly in time, has been known for decades to only be valid for sufficiently homogeneous systems. If the heterogeneity of the advecting velocity field is sufficiently large, either as a consequence of the porous medium's large heterogeneity [2] or due to the presence of another nonmiscible phase in the pore space [3–5], anomalous transport is observed, characterized by a spatial variance of

the transported plume that scales as a nonlinear power law of time. Another configuration in which anomalous transport can occur is when the transported species are partitioned between phases of different mobilities and can be exchanged between them. Such is the case in fractured media with a rock matrix in which solute species can diffuse [6,7] or in porous media with adsorption and/or desorption sites [8]. Other environmental processes can be described by similar mobile-immobile (MIM) or multirate mass transfer (MRMT) models, for example, the transport of sediment particles and sediment-borne substances in turbulent shear flows [9]. Whether normal or anomalous transport is observed macroscopically depends on the nature of the interaction between the different phases [10], and in particular on the statistical distribution of residence times in the different phases [10,11]. The main theoretical framework to characterize anomalous transport are continuous time random walks [12] and fractional advection-diffusion equations [9]. Note that anomalous transport is often associated to incomplete mixing at the pore scale, which can strongly impact reaction rates during reactive transport (see, e.g., Refs. [13,14]). In this paper, we characterize experimentally vapor transport in a porous material in which the mobile phase is transported through macro and mesopores of the material (in the range 100 nm to a few μm), while a "nearly immobile" phase resides in the nanopores (~1 nm).

The porous materials studied here are powders of a smectite clay, fluorohectorite. Smectite clays are among the most

*yves.meheust@univ-rennes1.fr
†jon.fossum@ntnu.no
‡geraldo@fis.unb.br

abundant minerals on the Earth's surface, found in rocks, sediments, and soils. They are also inexpensive and environmentally friendly materials. Their basic crystallographic unit is a quasi-two-dimensional (quasi-2D) crystallite denoted lamella. Nonperfect stoichiometry of the lamellae results in a structural negative surface charge. This surface charge is compensated by positive cations that are shared between lamellae, which results in the formation of stacks of lamellae with a nanosized quasi-2D interlayer space between them. In a dry or weakly hydrated smectite, the mineral grains (i.e., particles) consist of such nanostacks. In that weakly hydrated state the structure of a smectite clay mineral must thus be considered multiscale, the material consisting of aggregates of particles, which themselves consist of stacked lamellae [15,16]. Fluorohectorite (Fh), in particular, is a synthetic smectite which has often been used as a representative clean model system of natural smectites.

Smectite clays are also called *swelling* clays. Their ability to swell, which is mostly caused by their interaction with H_2O, has attracted much scientific and technological interest [17] in the past 40 years. Clay swelling is seen macroscopically as the increase in the material's apparent volume by its intake of liquid or gas, but it results from a microscopic process, namely the intercalation of foreign molecules, such as H_2O [18–21] or CO_2 [22–24], in the interlayer spaces within the smectite particles (i.e., nanostacks). The negative charges of the layers together with the presence of interlayer cations control the swelling dynamics [18,24,25]. The intercalation is quantified by the basal spacing or *d* spacing, which is the repetition distance of layers in a particle (i.e., nanostack) and is primarily controlled by the number of intercalated molecules. For H_2O molecules, particular molecular complexes and packings are energetically favored [26], which results in particular discrete values of *d* spacing, depending on the environmental conditions, i.e., primarily on relative humidity and temperature [27–30]. These discrete *d*-spacing values correspond to different hydration states of the clay particles, and are denoted *x*WL ($x = 0, 1, 2, 3, \ldots$), where WL stands for "water layers." The values of *d* spacings, as well as dynamics of the transitions between hydration states, are strongly impacted by the nature of the cations that allow nanostack particles to hold together. For fluorohectorite in particular, a number of hydration studies have been performed with different types of intercalated cations [19,28,31–33]. Among them, recent studies have shown that the dynamics of H_2O intercalation in LiFh (where the intercalated cation is Li^+) is markedly different from that in NaFh [24].

In the present work, we do not study the intercalation or swelling process in itself, but how it impacts the diffusion of water vapor through the mesoporous space of a clay powder that is prevented from swelling macroscopically. From the point of view of diffusive water transport, the multiscale structure of the clay can be considered a dual-porosity system, because diffusive transport through mesopores (between clay particles within aggregates) and macropores (between clay aggregates) is much faster than the transport through nanopores. There is to our knowledge no data available for the diffusion coefficient of any molecule or ion in the interlamellar (nanoporous) space of fluorohectorite. However, a compilation of the values found in the literature for

montmorillonite (see Appendix A), the natural hectorite that is the most similar to fluorohectorite, shows that the molecular diffusion coefficient of H_2O in the interlamellar space of Li montmorillonite and Na montmorillonite is more than four orders of magnitude smaller than that of vapor in air at room temperature. Even if confinement decreases the mesoporous molecular coefficient diffusion of water in vapor phase by one or two orders of magnitude, it remains much larger than that of water molecules in the interlamellar space. Hence, when water vapor is transported through uncompacted powder material, water molecules can be considered to diffuse through the meso and macropores, while possibly intercalating into nanoporous clay grains, where their diffusive transport can be neglected. This coupling between a traveling water phase and the water phase trapped in the nanopores through an exchange mechanism is reminiscent of mobile-immobile (MIM) models mentioned above and frequently used to describe subsurface transport processes, except that here the trapping occurs at a much smaller, nanometric, scale. Hence, depending on the dynamics of the trapping process, we may expect to observe anomalous (i.e., non-Fickian) transport.

The diffusive transport of water molecules in vapor phase is of particular interest since the low permeability of clays does not allow for the intake of a significant liquid phase. Vapor transport has obvious soil relevance, as well as subsurface applications in enhanced oil recovery (EOR), such as steam EOR [34]. Vapor transport through smectite clays such as bentonite may also have effects in situations where clays are used as barrier materials for contaminant confinement such as heavy metals or nuclear waste [35]. Quantitative characterization of gas transport in porous media is not easily achieved. Cousin *et al.* [36] have estimated the diffusion coefficient of air in a silty-clay soil with a setup based on the counting by a scintillation counter of radioactive molecules mixed with the air. Imposing a permanent gradient of humidity between the two ends of a dry sample of Na-fluorohectorite (NaFh) smectite clays, Løvoll *et al.* [37] monitored the advancement in time of the intercalation front using x-ray diffraction. The front advancement was shown to scale as $\sqrt{t}$ [38], as expected for a standard diffusive process. Hemmen *et al.* [39,40] performed a similar experiment coupled to an equilibration experiment in which the *d* spacing was mapped to the relative humidity value in the vicinity of clay grains. This study, performed with the same kind of NaFh samples as in the present study, provided longitudinal profiles of locally averaged relative humidity in the clay mesopores at regular time intervals. The time evolution of those profiles can be modeled through a one-dimensional normal diffusion process, thus demonstrating that H_2O vapor transport through a NaFh powder, i.e., with Na^+ as an interlayer cation, can be described by normal Fickian diffusion [39,40], in good consistency with the $\sqrt{t}$ scaling mentioned above.

In this study we have performed the same type of experiments as Hemmen *et al.* [39,40], now on two types of synthetic smectites: Na fluorohectorite (already studied by Hemmen *et al.*) and Li fluorohectorite (LiFh). Our purpose is to investigate mesoscopic transport of water molecules in initially dry fluorohectorite clays, and how it is impacted by the properties of the trapping of an immobile phase inside the nanopores. The trapping mechanism, namely water intercalation into clay
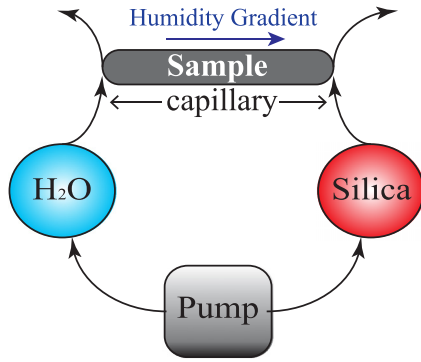
FIG. 1. Sketch of the experimental setup. The H_2O vapor is generated by pumping air into a container filled with water while the dry air is generated by pumping air into a container filled with silica gel. The pressure on both ends is the same, so the only transport mechanism is diffusion.

grains, has a very different dynamics in LiFh as compared to NaFh.

II. METHODS

A. Clay samples

The Li-fluorohectorite (LiFh) clay mineral used in the experiments was purchased from Corning Inc. and Na fluorohectorite (NaFh) was obtained from LiFh through a cation exchange process. Both samples have a nominal chemical formula $M_{1.2}(Mg_{4.8}Li_{1.2})Si_8O_{20}F_4$, where M is the interlayer cation (Li^+ or Na^+ in the present case). Note that these fluorohectorites are the same materials as those used in Refs. [19,24,39].

B. Transport experiments

Loosely packed powder samples of LiFh and NaFh were placed inside a glass capillary of diameter 1 mm, with both ends open. The capillary prevents macroscopic swelling of the clay samples. The capillary was then mounted in a sample holder, which was connected to an open circuit at each end. To generate humid and dry air the circuits went through a container filled with H_2O and silica gel, respectively, and a peristaltic pump was used to pump air into the circuits. The relative humidity (RH) measured in each circuit was $\simeq 97\%$ for the H_2O circuit and $\simeq 0\%$ for the dry circuit. Both ends of the capillary were submitted to the same pressure in order to prevent pressure gradient driven transport (advection or convection), so that the only transport mechanism is diffusion. Figure 1 shows a sketch of the experimental setup.

The basic tool for experimentally characterizing crystalline swelling is x-ray diffraction (XRD) [20,27,28,31], which allows monitoring the stepwise change of the (001) d spacing as a shift in diffraction peak positions. X-ray diffraction (XRD) measurements of the intercalation dymanics that are presented in Sec. III A were performed at the Brazilian Synchrotron Light Source Laboratory (LNLS) at the XRD2 beam line, using a wavelength $\lambda = 0.155$ nm. The transport experiments (see Sec. III B and onwards) were performed at NTNU (Trondheim, Norway) using an in-house Bruker

NanoSTAR x-ray scattering instrument, attached to a Xenox stationary electron impact source with a copper anode, producing K_α radiation. The scattered intensity was recorded by a two-dimensional multiwire grid Xe gas detector (HI-STAR, Bruker). The beam diameter of the setup is 400 μm and the detectable range of momentum transfer q is $2.5 < q < 7.5$ nm^{-1} [q is classically defined as $q = (4\pi/\lambda)\sin\theta$, where θ is the scattering angle and λ is the wavelength of the x rays]. The relation between q and the corresponding length scale d is $d = 2\pi/q$, which means that the range of investigated length scales is between 0.84 and 2.5 nm. In the diffractograms, the peaks characteristic of diffraction by the one-dimensional periodic structure of the layers are identified. The position of the first order peak, which is also the one with the largest intensity, provides a length scale which is the average d spacing of the grains that are present in the scattering volume, that is, the volume of the sample intersected by the x-ray beam.

The two-dimensional detector provides the azimuthal dependence of the diffraction peaks. That dependence can be used to measure the probability density function (PDF) of clay particle orientations in the sample [38]. Using this procedure (data not shown) we have observed that the clay powder is not isotropic in the capillary, but that the PDF of clay particle orientations does not vary along the length of the sample. Hence this anisotropy is not expected to impact the longitudinal water transport in any way.

The samples were first dehydrated by heating for one day in an oven at a temperature of 120 °C. The initial hydration state of the clay particles in the sample was then 0 WL (dehydrated sample). At the time considered $t = 0$ s for the experiment, one end of the sample was connected to the wet circuit and reservoir at RH $\simeq 97\%$, the other remaining connected to the dry air circuit. Details of this procedure can be found in Ref. [37]. The pressure difference between the wet and dry end of the sample was recorded in time and remained negligible during the entire experiment [41].

C. Transport model

In the experiment, H_2O diffuses through a porous medium packed in a thin and long glass capillary and measurements are performed at times at which the diffusing H_2O molecules remain far from the end of the sample that is in permanent contact with the dry circuit. In order to interpret the data, we can therefore consider a one-dimensional Fickian diffusion process of W, the mass density of the diffusing species in the mesoporous space, in a semi-infinite system with $W(x \rightarrow \infty, t) = 0$, x and t being the space and time coordinates, respectively. Note that the relative humidity (RH) is the ratio of the partial pressure of the H_2O vapor to the equilibrium vapor pressure of H_2O. Therefore, it is proportional to the mass density $W(x, t)$ of the diffusing species. The time evolution of W is described by a nonlinear diffusion equation [42] in the form

$$\frac{\partial W}{\partial t} = \frac{\partial}{\partial x}\left[D(W)\frac{\partial W}{\partial x}\right],\qquad (1)$$

where $D(W)$ is the normal Fickian diffusivity (or diffusion coefficient) assumed to be a function of W only.

The humidity reservoir is placed at $x \leqslant 0$ and imposes $W(0,t) = W_0$ at any time $t > 0$, while at $t = 0$ the sample is perfectly dry. The boundary and initial conditions for the transport process thus read

$$\begin{cases} W(x=0,t) = W_0, & \forall t > 0, \\ W(x \to \infty, t) = 0, & \forall t, \\ W(x, t=0) = 0, & \forall x > 0. \end{cases} \quad (2)$$

From now on, we choose to consider the function $\Phi = W/W_0$, which also verifies Eq. (2), with boundary conditions

$$\begin{cases} \Phi(x=0,t) = 1, & \forall t > 0, \\ \Phi(x \to \infty, t) = 0, & \forall t, \\ \Phi(x, t=0) = 0, & \forall x > 0. \end{cases} \quad (3)$$

For such boundary conditions, a classic variable change (Boltzmann's transformation) [42], $\eta = x/\sqrt{t}$, allows rewriting Eq. (1) as a function of η alone:

$$-\frac{1}{2} \eta \frac{d\Phi}{d\eta} = \frac{d}{d\eta}\left(D(\Phi)\frac{d\Phi}{d\eta}\right). \quad (4)$$

The boundary conditions can also be expressed in terms of the single variable η, for $t > 0$:

$$\Phi(\eta = 0) = 1, \quad \Phi(\eta \to \infty) = 0. \quad (5)$$

Since Eq. (4) and the initial and boundary conditions of Eq. (5) are functions of η alone, the same holds for $\Phi(\eta)$. Consequently, when the profiles are plotted as functions of the scaling variable η, they are expected to collapse on a single universal curve. Furthermore, the diffusion coefficient can then be obtained from the knowledge of the function $\Phi(\eta)$ [42]:

$$D(\Phi) = -\frac{1}{2}\left(\frac{d\eta}{d\Phi}\right)\int_0^{\Phi} \eta(\Phi')d\Phi'. \quad (6)$$

If the diffusion profiles do not collapse, it means that Fickian diffusion is not an appropriate model for the observed vapor transport [43,44]. In that case a generalization of Eq. (1) is required. One type of anomalous diffusion is characterized by a time evolution of the mean square displacement $\langle(\Delta x)^2\rangle(t)$ in the following form [44–46]:

$$\langle(\Delta x)^2\rangle = \frac{2D_\gamma\, t^\gamma}{\Gamma(1+\gamma)}, \quad (7)$$

where $0 < \gamma < 1$ (as opposed to $\gamma = 1$ for standard Fickian diffusion). Such anomalous diffusion processes are described by a fractional time diffusion equation:

$$\frac{\partial^\gamma W}{\partial t^\gamma} - \frac{t^{-\gamma}}{\Gamma(1-\gamma)}W(x,0) = \frac{\partial}{\partial x}\left(D\gamma(W)\frac{\partial W}{\partial x}\right), \quad (8)$$

where Γ is defined by $\Gamma(y) = \int_0^\infty x^{y-1}e^{-x}dx$ and $\partial^\gamma/\partial t^\gamma$ is the Riemann-Liouville fractional derivative operator defined as

$$\frac{\partial^\gamma W(x,t)}{\partial t^\gamma} = \frac{1}{\Gamma(1-\gamma)}\frac{\partial}{\partial t}\int_0^t \frac{W(x,t')}{(t-t')^\gamma}\,dt'. \quad (9)$$

Considering the function Φ as defined above and changing the variables to $u = t'/t$ and $\eta = x/t^{\gamma/2}$, one obtains from Eq. (8)

[47,48]

$$\frac{1}{\Gamma(1-\gamma)}\int_0^1 \left[(1-\gamma)\Phi\left(\frac{\eta}{u^{\gamma/2}}\right) - \frac{\gamma}{2}\eta\frac{\partial\Phi\left(\frac{\eta}{u^{\gamma/2}}\right)}{\partial\eta}\right]$$

$$\times \frac{du}{(1-u)^\gamma} = \frac{\partial}{\partial\eta}\left(D_\gamma(\Phi)\frac{\partial\Phi}{\partial\eta}\right). \quad (10)$$

In this case the scaling of the humidity profiles onto a single master curve still holds provided that the scaling parameter be defined as $\eta = x/t^{\gamma/2}$.

Defining a new variable $\xi = \eta/u^{\gamma/2}$, the dependence on Φ of the generalized diffusion coefficient, $D_\gamma(\Phi)$, can also be calculated, from the following expression which generalizes Eq. (6):

$$D_\gamma(\Phi) = \frac{d\eta}{d\Phi}\frac{1}{\Gamma(1-\gamma)}\int_0^\eta d\eta'\int_{\eta'}^\infty$$

$$\times \left(\frac{2}{\gamma}(1-\gamma)\frac{\Phi(\xi)}{\xi} - \frac{d\Phi(\xi)}{d\xi}\right)\frac{\left(\frac{\eta'}{\xi}\right)^{\frac{2}{\gamma}}d\xi}{\left[1-\left(\frac{\eta'}{\xi}\right)^{\frac{2}{\gamma}}\right]^\gamma}. \quad (11)$$

III. RESULTS AND DISCUSSIONS

A. From intercalation state to relative humidity profiles

The relative humidity (RH) inside the mesoporous space of the sample in the vicinity of the mineral grains that are contained in the x-ray scattering volume can be estimated from a fine measurement of the average d spacing for those grains. In order to know how the interlayer spacing and RH are related, we have performed a separate quasistatic calibration experiment, in which a small volume of the sample is exposed to precisely controlled relative humidity under conditions otherwise identical to those in the transport experiment, in particular at the same temperature. In this quasistatic experiment, the humidity is raised in steps, and the d spacing is given time to equilibrate between RH steps. The details of the procedure are given in Refs. [18,39]. The x-ray diffractograms recorded for each type of stable hydration states are given in Fig. 2(a) for NaFh and Fig. 2(b) for LiFh.

The $d(RH)$ relationship shown in Fig. 2(c) [respectively, 2(d)] is obtained by measuring the position q_c of each Bragg peak in the plots of Fig. 2(a) [respectively, 2(b)] as a function of RH and using the relation $d_c = 2\pi/q_c$. The plateaus shown in Figs. 2(c) and 2(d) then correspond to the various hydration states. The number of intercalated water molecules increases with RH [18,32]. In particular, the plateaus are not strictly horizontal; rather they exhibit a slow monotonically increasing dependence on RH, which can be measured with a resolution of 0.1 Å or better. For NaFh three hydrodynamically stable hydration states are reported: $\simeq 1.0$ nm, $\simeq 1.2$ nm, and $\simeq 1.5$ nm, denoted zero H_2O layer (0 WL), one H_2O layer (1 WL), and two H_2O layers (2 WL), respectively [19,27,28,32,39]. Similarly, LiFh exhibits the 0 WL, 1 WL, and 2 WL hydration states, but also an additional state at $\simeq 1.4$ nm, the so called one-and-a-half H_2O layer (1.5 WL) in between the 1 WL and 2 WL states, as well as another state at $\simeq 1.9$ nm, the 3 WL hydration state. The d spacing can change significantly due to hysteresis behavior, depending on whether
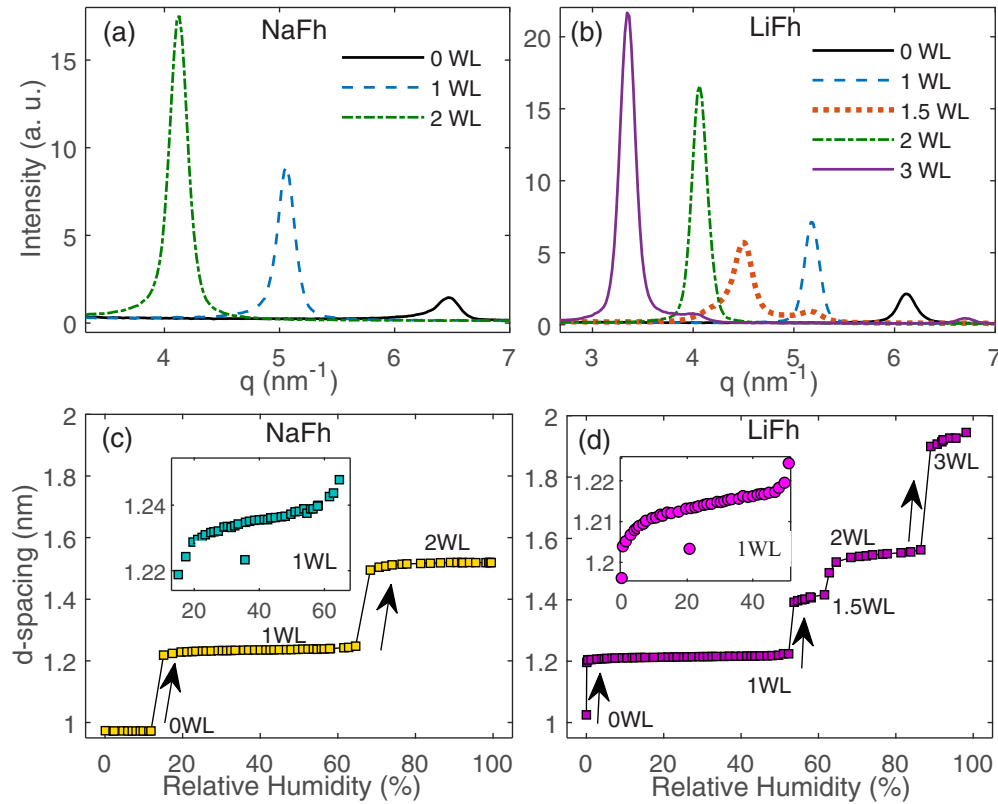
FIG. 2. X-ray diffractograms recorded for the stable hydration states of (a) NaFh and (b) LiFh. For NaFh the stable hydration states are 0, 1, and 2 WL, while for LiFh the stable hydration states are 0, 1, 1.5, 2, and 3 WL (c) d spacing as a function of RH for (c) NaFh and (d) LiFh. The stable hydration states correspond to the plateaus, while the sharp increases between them denote the hydration transitions. The inset shows a zoom of the 1 WL region for both samples.

the material is being hydrated or dehydrated [28,39]. Since in the present work the material is only hydrating, the hysteresis effect is not relevant.

In order to measure the time scale of the intercalation of H_2O into the NaFh and LiFh samples, the growth of the Bragg peak corresponding to the 1 WL hydration state was recorded as a function of time. Figure 3 shows the time evolution of the intensity, normalized to the saturation value, of the 1 WL
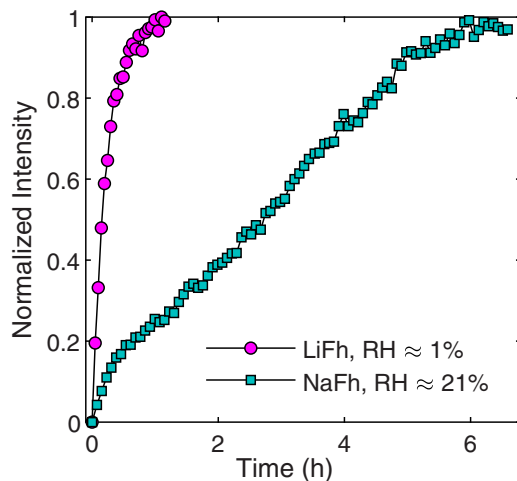

FIG. 3. Normalized intensity of the Bragg peak corresponding to the 1 WL region during the hydration transition from 0 WL to 1 WL.

peak for LiFh and NaFh. For LiFh the transition to 1 WL starts at RH < 1% and stabilizes within $t \simeq 1$ h, while for NaFh the expansion is initiated at RH > 20% and stabilizes after $t \simeq 6$ h. As observed, intercalation of H_2O into LiFh is faster and occurs at RH conditions much lower than for the intercalation of H_2O into NaFh.

B. Spatiotemporal evolution of the d spacings

The d spacings of NaFh and LiFh are shown in Fig. 4 as a function of time during the transport experiments, for all measurement positions along the capillary. The measurement positions are 1, 2, 3, . . . , 19 mm, but for the sake of clarity only plots corresponding to measurement positions described by odd numbers are shown with symbols linked by a continuous line, and mentioned in the legend. Plots corresponding to measurement positions described by even numbers are only shown as dotted lines. Each of the plateaus observed in Fig. 4 corresponds to a hydration state and the transitions between hydration states are observed to behave in a stepwise manner, as explained in Sec. I and observed as a function of relative humidity in Figs. 2(c) and 2(d).

C. Relative humidity profiles

The relative humidity $RH_x(t)$ was computed from $d_x(t)$ using the calibration data obtained in the separate equilibration hydration experiment, as explained above in Sec. III A.
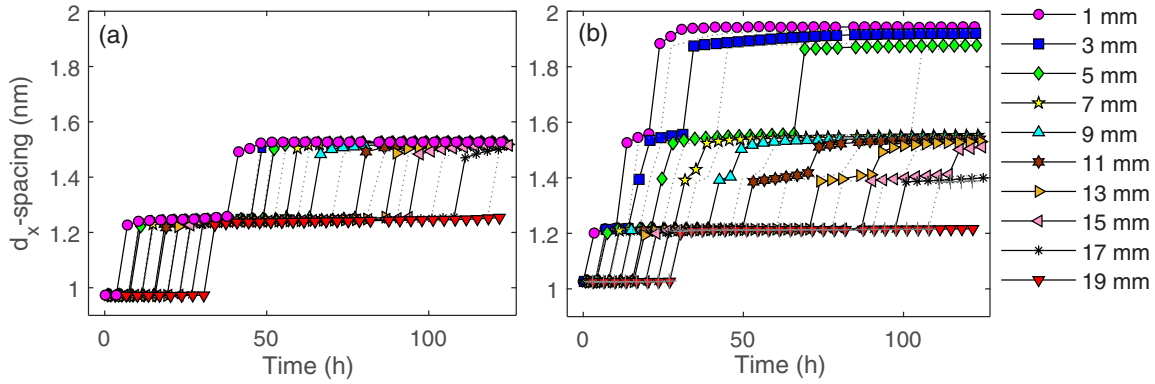
FIG. 4. d spacing as a function of time for 19 spatial coordinates along the quasi-one-dimensional sample. The positions are separated by 1.0 mm and the distance is measured from the humid end of the sample. For the sake of clarity, the plots corresponding to measurement positions described by even numbers (namely, 2, 4, 6, . . . , 18 mm) are only shown as dotted lines and not referenced in the legend.

This procedure was found to be satisfactory since H_2O vapor transport in clay minerals is rather slow ($\sim$ cm/days), while the d spacing was seen to stabilize much faster when varying the RH. The results of the conversion, i.e., the time evolution of the relative humidity as a function of time for the various longitudinal positions at which it was recorded, are shown in Fig. 5. The humidity profiles in Fig. 5 have a shape characteristic of a diffusion process. The $x = 0$ represents the side close to the H_2O vapor reservoir. The lowest curve in the plots corresponds to the beginning of the experiment ($t = 0$) and the others have been recorded with a 3 h time interval, up to $t = 80$ h. Each curve was fitted by a smoothing spline function, shown as a line in the figure. For the sake of clarity, the data corresponding to measurement positions described by odd numbers are shown as symbols, with fitting curves shown as solid lines, while for measurement positions described by even numbers only the fitted curve is shown, as a dotted line.

These fitted spline functions were then used to construct the spatial variation $RH_t(x)$ of the RH, at any given recording time t, from the time-dependent data $RH_x(t)$. The results are shown in Fig. 6. The spatial humidity profiles in Fig. 6 have a shape characteristic of a diffusion process. $x = 0$ represents the side close to the H_2O vapor reservoir. The lowest curve in the plots corresponds to the beginning of the experiment ($t = 0$) and the others correspond to times regularly spaced, with a 3 h time interval, up to $t = 80$ h. For the sake of clarity, only plots corresponding to measurement times that are a multiple of 9 h are shown with symbols; the others are shown as dotted lines and not referenced in the legend of the figure.

D. Collapse of humidity profiles

The spatial humidity profiles of Fig. 6 are plotted in Figs. 7(a) and 7(b) as a function of the scaling parameter $\eta = x/t^{\gamma/2}$, with $\gamma = 1$. For NaFh the collapse of the curve with $\gamma = 1.00 \pm 0.02$ is satisfactory. It is the γ value that best collapses the NaFh data on a master curve [Fig. 7(a)], which shows that, within experimental resolution, H_2O transport through NaFh is a normal (Fickian) diffusion process. For LiFh, however, no good collapse of the humidity profiles can be achieved with $\gamma = 1$ [Fig. 7(b)]. This indicates that the transport process cannot be described by normal diffusion. For LiFh the best collapse in this particular experiment is obtained

for $\gamma = 0.67 \pm 0.02$, shown in Fig. 7(c). It is characteristic of a significantly subdiffusive process; hence there is a fundamental difference between NaFh and LiFh when it comes to diffusive H_2O vapor transport.
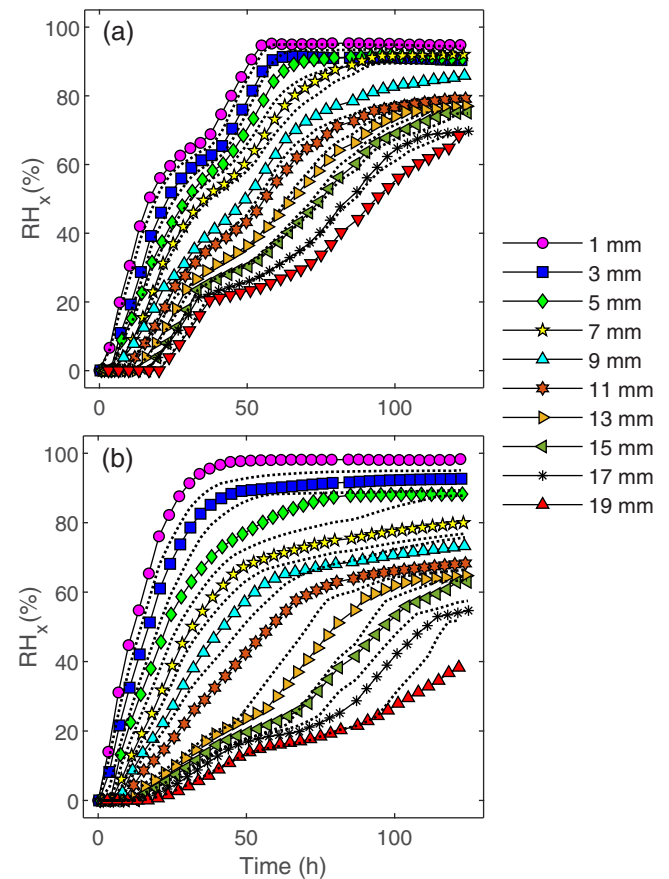

FIG. 5. Evolution of the RH as a function of time. Each curve corresponds to a spatial position x along the sample. $x = 0$ corresponds to the sample end in contact with the H_2O reservoir. The continuous lines denote spline functions which were fitted to the data. The dotted lines are splines fitted to data measured at measurement positions described by even numbers ($x = 2, 4, \ldots, 18$ mm), for which data symbols are not shown to enhance the figure's clarity.
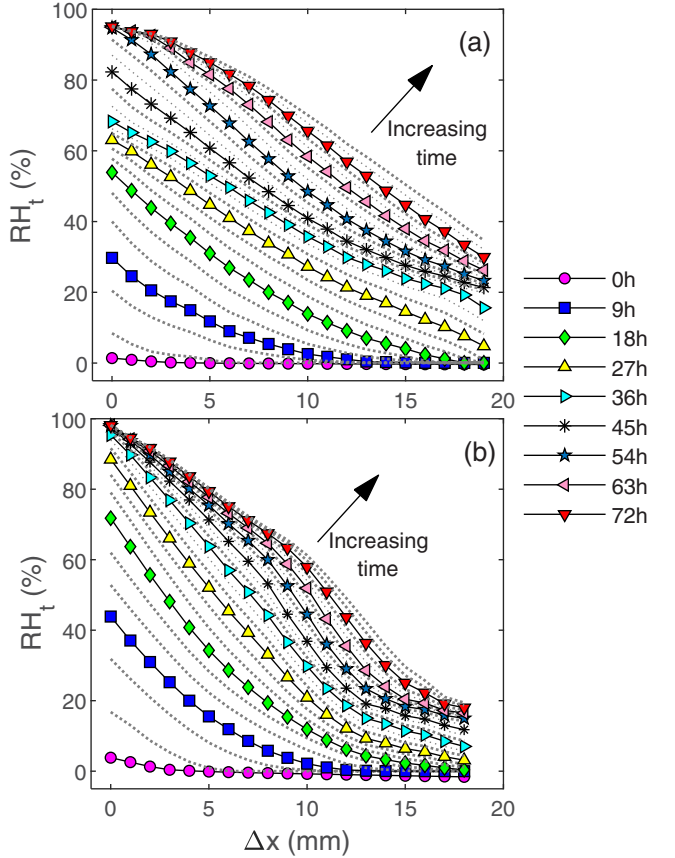
FIG. 6. Relative humidity plotted as a function of position (Δx), for measurement times separated by a 3 h time interval. The plots corresponding to the measurement times referenced in the legend (i.e., which are multiples of 9 h) are shown as symbols linked by a solid line, while the others are simply shown as dotted lines, to enhance the figure's clarity.

E. Dependence of the diffusion coefficient on the relative humidity

From the collapsed plots of Fig. 7, we define a single master curve. To discriminate local fluctuations of the derivatives arising from experimental uncertainties we fit that master
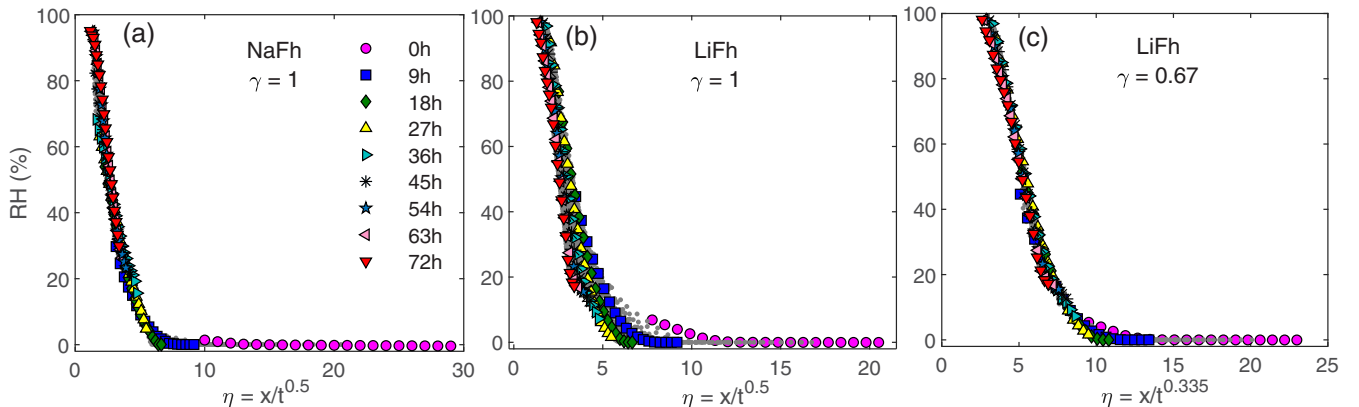
curve with an analogous formula of the form

$$\Phi(\eta) = \frac{1 - \operatorname{erf}\!\left(\frac{\eta - \eta_0}{a}\right)}{1 + \left(\frac{\eta}{b}\right)^n}, \qquad (12)$$

where η_0, a, and n are fitting parameters. A reciprocal relationship $\eta(\Phi)$, defined on the range between zero and 1, is then obtained numerically from the analytical formula (12). From this relationship we compute numerically the dependence $D(\Phi)$ of the dispersion coefficient on the normalized relative humidity for NaFh, using Eq. (6). Similarly, $D(\Phi)$ for LiFh is obtained from the functional forms of both $\eta(\Phi)$ and $\Phi(\eta)$ using Eq. (11). The results for NaFh and LiFh are shown in Figs. 8(a) and 8(b), respectively. Note that the values are approximately four orders of magnitude smaller than the diffusion coefficient of water vapor in air (2.82×10^{-5} m^2/s) [49], which is expected due to the confinement of the water molecules in the porosity of the medium.

F. Scaling of the intercalation front position with time

Since H$_2$O transport in NaFh is described by a normal effective longitudinal diffusion (previously observed by Hemmen *et al.* [39]), the advancement of the intercalation front (1 WL to 2 WL) is expected to scale as $\sqrt{t}$ [39]. This advancement of the intercalation front Δx_{front} is the position at which the humidity is sufficiently large to make the system undergo a transition between the dehydrated state to the monohydrated state. Thus the humidity value for the intercalation front is RH = 21% for NaFh and RH = 1% for LiFh, as shown in Fig. 3. The time evolution of $x_{\text{front}} = \Delta x(W = 21\%)$ for NaFh is shown in Fig. 9(a) and does indeed scale as $\sqrt{t}$. For LiFh the front position is $x_{\text{front}} = (\Delta x)^{1/\gamma}(W = 21\%)$ and its expected scaling is in the anomalous form $t^{\gamma/2}$ with $\gamma = 0.67$, which is verified by the data in Fig. 9(b). These results are in fact expected from the collapses in Figs. 7(a) and 7(c), respectively.

IV. DISCUSSION

A. Mechanisms at play vs effective 1D transport model

We have studied the one-dimensional (1D) transport of moisture through an initially dry smectite clay powder. In

FIG. 7. *RH* plotted as a function of the scaling parameter $\eta = x/t^{\gamma/2}$, where for (a) NaFh $\gamma = 1$. (b) For LiFh, $\gamma = 1$ does not collapse the humidity profiles. (c) Humidity profiles of LiFh collapsed with $\gamma = 0.67 \pm 0.02$, which is characteristic of a subdiffusive transport process.
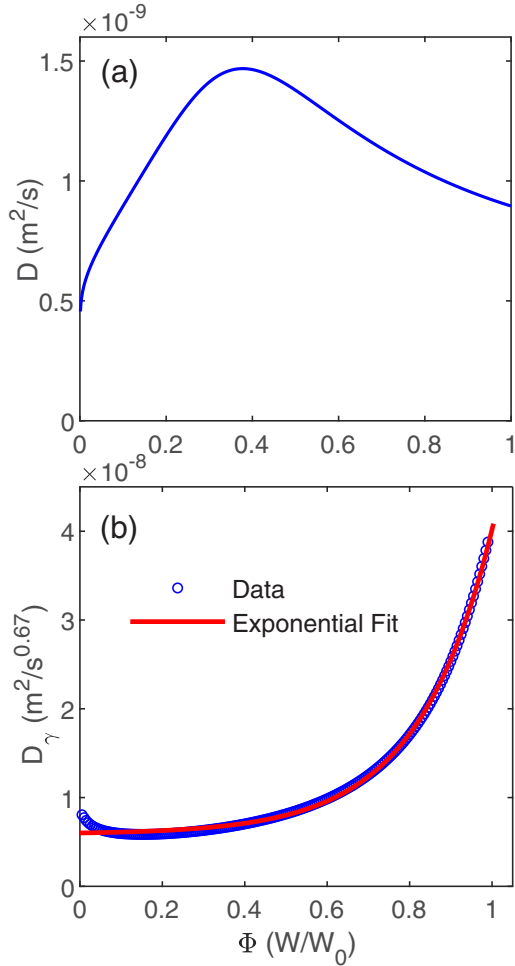
FIG. 8. Dependence of the diffusion coefficient on the relative humidity normalized by its value at the boundary with the wet reservoir. For NaFh (a), the plot corresponds to the relation of Eq. (6), while for LiFh (b), it corresponds to that of Eq. (11), which could be fitted with an exponential function (red curve) on most of the Φ range.

addition to the diffusion of H_2O molecules in gas phase through mesopores, the microscopic transport mechanisms at play can involve surface diffusion, associated with H_2O adsorbed on the surface of pore walls, or possibly the formation of H_2O microdroplets due to condensation of vapor in parts of the system [50,51]. In the latter case, the vapor pressure difference between both sides of an H_2O droplet can lead to evaporation at one end and condensation at the other end. As explained in the Introduction, these processes taking place in the mesoporous space are coupled to the intercalation of water molecules into the nanoporous space. During this intercalating process, not only are H_2O molecules removed from the mesoporous environment, but they also increase the clay particles' thickness. As the macroscopic swelling of the samples is prevented in our experimental setup, water intercalation into the nanopores results in a decrease of the mesoporous space available to the transported H_2O molecules: the nano- and mesoscales are thus highly intercoupled [52]. Hence these two effects, trapping by intercalation and its associated mesoporous space reduction, mostly control the nature of H_2O transport through the smectite clays. The swelling is also accompanied by the separation of clay grains into grains containing less clay platelets. That is, the average thickness of, or equivalently the number of clay platelets contained in, a clay particle decreases when the hydration state is changed to a more hydrated configuration (see Appendix B).

In order to assess the Fickian vs anomalous nature of the mesoporous 1D transport though the medium, we have used a diffusion model involving an exponent γ characteristic of the anomalousness of the transport and a diffusion coefficient, D_γ, that is a function of the local H_2O vapor concentration only. This effective description encompasses all the mechanisms presented above, combined with the constraint of mass conservation and Fick's law for H_2O molecules in the gas phase, as well as the particular geometry of the medium (powder of anisotropic clay particles in the present case; see Sec. II B). How the dynamics of H_2O intercalation into the clay particles controls the 1D mesoporous diffusive process can be understood along the following lines. At a given time and location in the sample, if the relative humidity reaches the threshold value at which intercalation into nanopores occurs,
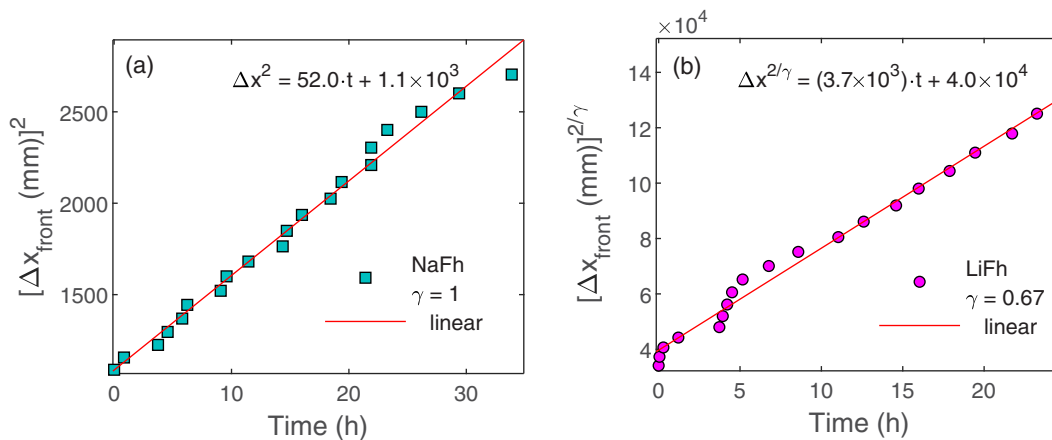

FIG. 9. Position of the intercalation front from 0 WL to 1 WL as a function of time. For NaFh (a) the position of the front is proportional to $\sqrt{t}$ (represented as the solid lines), as expected from normal diffusion. For LiFh (b) the same scaling holds for $x_{\text{front}}^{1/\gamma}$.

the removal of water molecules from the mesoporous space by this intercalation, combined with the associated reduction in mesoporous space, can result either in an effective local increase or a decrease of Φ, since those two effects have opposite impacts on Φ. If there is an increase of Φ, also the local Φ gradient will increase since, ahead of the location in question, intercalation conditions have not been reached yet, and diffusion will thus be enhanced locally. On the contrary, if the net result of local intercalation is a decrease in Φ, then diffusion may be expected to be impeded locally.

B. Why different behaviors for NaFh and LiFh?

Complex interactions between the diffusing species and the medium components generally lead to non-Markovian subdiffusive behavior [47,53–55]. This is indeed what we observe for LiFh, but not for NaFh. One important factor in this context is that LiFh particles expand $\simeq 20\%$ more than NaFh particles along the d-spacing direction (see Fig. 4). In the light of the arguments presented in Sec. IV A above, LiFh particle swelling may well enhance mesoporous diffusion where it occurs, while NaFh particle swelling may act in the opposite direction. It is however likely that more dynamic effects such as the difference in intercalation dynamics play a role in the difference between the $D(W)$ curves for NaFh and LiFh. Indeed, Fig. 3 shows that the LiFh powder adsorbs H_2O approximately six times faster than the NaFh powder, and at lower humidity values.

C. Independence of γ and the functional form of $D_\gamma(\Phi)$ from the hydration state

Since the swelling of the clay particles reduces the permeability of the mesoporous space, one may have expected the effective diffusion process to depend on the hydration state. In particular, the generalized Boltzmann-Matano analysis presented in Sec. II C can be performed separately on the experimental data corresponding to each hydration state of the considered clay material. It turns out that doing so yields values of the exponent γ, for all hydration states, that are not very different from the value obtained from a global collapse, as presented above. Considering that such collapses, performed over a small portion of the RH spatial profiles, are prone to a larger uncertainty than a collapse over the entire range of relative humidities, we have concluded that a diffusive transport process controlled by a single global exponent γ is the theoretical description that is best suited to our data. Consequently, the functional form of $D_\gamma(\Phi)$, given by Eq. (11), is the same for all hydration states.

D. Is the value of γ universal?

Interestingly, the exponent γ measured in zeolites is not universal but depends on the sample preparation (in particular, thermal) history [47]. Similar conclusions regarding experimental history were reported in a work on the synthetic smectite laponite [56]. Memory effects are incorporated in the value of the fractional exponent γ, and for zeolites this has been reported to become all the more important as the value of γ is smaller [47].

Here, for LiFh and for an initial condition RH $\simeq 63\%$ at the humid side (data not shown here), we found an exponent value of $\gamma = 0.33$, to be compared to the exponent 0.67 reported in Sec. III D. This indicates that the exponent value for LiFh is not universal and could be influenced by the sample preparation history or different boundary conditions. As pointed out by Neaman *et al.* [57], the different procedures of compression, heating, and hydration affect the textural properties of the clay mineral system. However, due to the strong and fast interaction between the diffusing species and the medium, we expect transport to always be anomalous for LiFh. In contrast, the NaFh sample studied here was preheated to $120\,°C$ until dehydrated, and this resulted in normal diffusion transport with $\gamma = 1$. Hemmen *et al.* obtained approximately the same value for γ in a similar NaFh system at $15\,°C$, which was initially in the 1 WL hydration state [39]. This result suggests that sample preparation history in NaFh has little effect on the water vapor transport through the mesopores.

E. Behavior of $D_\gamma(\Phi)$

Figure 8 shows the $D_\gamma(\Phi)$ (with $\Phi = W/W_0$) relationships calculated from the measured humidity profiles, for NaFh and LiFh. For NaFh the relationship increases continuously with Φ at low humidity values, goes through a maximum around $\Phi \simeq 0.36$, and decreases continuously at humidity values larger than the maximum value. This is due to the preference of Na smectites for the expanded hydrated states [58]. For LiFh, on the contrary, the relationship is mostly continuously increasing, with the exception of very small relative humidity values. For $\Phi > 0.3$ this can be fitted with an empirical exponential function of the form $D_\gamma(\Phi) = D_\gamma^{(0)} \exp(\alpha\Phi)$ with $D_\gamma^{(0)} = (1.33 \pm 0.05) \times 10^{-10}$ m^2/s$^{0.67}$ and $\alpha = 5.55 \pm 0.04$. Similar exponential behaviors of $D_\gamma(W)$ have been observed in other systems [59], in particular in a study of water transport through zeolite powders [47].

F. Practical consequences and applicability to natural environments

The results of this study have important practical consequences for subsurface applications of clay minerals such as caprock for the storage of CO_2 or containment material for nuclear waste. Let us for example consider the advancement of the swelling front shown in Fig. 9, and assume a 1 m length of our clay material; the time for H_2O molecules to diffuse through it would be approximately 2.2 years for NaFh and 28 years for LiFh. Hence the sensitivity of the mesoporous transport to the nature of the intercalated cation results in a one order of magnitude difference in the time needed for water molecules to penetrate 1 m of the clay material. This is mostly due to the difference in the exponent γ.

Note that in real applications the material would be much more compacted. Because of this, and due to the slight hydrophobicity of the lateral surface of fluorohectorite crystallites [31] as compared to natural, nonfluorinated, clays, the present results cannot be directly translated into predictions of diffusive transport times in clay material used to confine nuclear waste, for example. However, since the hydration dynamics of hydroxylated hectorites is faster than that of

TABLE I. Diffusion coefficients in the interlayer space (nanopores) of montmorillonite clays with either Li^+ or Na^+ as the intercalated cation, for the three possible hydration states. The values given for measurements by quasielastic neutron scattering (QENS) and predictions based on molecular dynamics (MD) simulations are those reported by Chang *et al.* [61], except when a reference is explicitly given.

Type of clay and	Li montmorillonite			Na montmorillonite		
hydration state	1 WL	2 WL	3 WL	1 WL	2 WL	3 WL
QENS measurements (m^2/s)	$(0.5–4) \times 10^{-10}$	$(2.6–7.0) \times 10^{-10}$	1.0×10^{-9}		1.0×10^{-9} $(0.9 \pm 0.1) \times 10^{-9}$ [25]	
MD predictions (m^2/s)	1.3×10^{-10}	4.5×10^{-10}	1.4×10^{-9}	1.0×10^{-10} 1.0×10^{-10} [60,62]	7.9×10^{-10} 1.0×10^{-9} [60,62]	7.3×10^{-10}

fluorohectorite, and since they incorporate more water in the interlayer space of the clay grains [31], we expect the mechanism responsible for anomalous mesoporous transport to be even more efficient in natural smectite clays, for the same given intercalated cation.

V. CONCLUSION AND PROSPECTS

The mechanism responsible for anomalous transport in this system is reminiscent of retardation mechanisms known for other types of subsurface media in which, as mentioned in the Introduction, the transported species are partitioned between a mobile phase and an immobile phase interacting with each other. However, the present retardation mechanism differs from the trapping mechanisms classically encountered in hydrological systems in at least two aspects. It involves (i) a nanoscale trapping mechanism (the intercalation), rather than a mechanism involving molecular diffusion at the hydrodynamic scale, and (ii) a feedback effect of the local concentration of the diffusing species on the porosity and permeability of the mesoporous space through which it is transported, due to intercalation-triggered particle swelling. The resulting mesoporous transport is Fickian for NaFh but markedly subdiffusive for LiFh. Mobile-immobile models yield subdiffusive transport of the mobile phase when the exchange (i.e., trapping) mechanism between the two phases involves a power law distribution of the trapping times [10,11]; the associated deterministic description is then a fractional (advection-)diffusion equation [9]. One interesting prospect of this study would thus be to characterize trapping time distributions in the nanolayered clay grains. Molecular diffusion numerical simulations would be the appropriate tool (see, e.g., Ref. [60]), but, to the best of our knowledge, no such study has ever addressed trapping time distributions. Note however that while such a power law distribution of waiting times could be responsible for part of the observed anomalous behavior, the feedback effect (ii) on porosity and permeability also plays a role, as the dependence of the γ value on the sample preparation history, discussed above, cannot be explained by the properties of the nanoscale trapping mechanism alone.

ACKNOWLEDGMENTS

APPENDIX A: VALUES OF DIFFUSION COEFFICIENTS FOR WATER IN THE NANOPORES OF SMECTITE CLAYS AND IN AIR

There is to our knowledge no data available for the diffusion coefficient of any molecule or ion in the interlamellar (nanoporous) space of fluorohectorite. But such values exist for montmorillonite, which is the natural clay that is the most similar to fluorohectorite. A compilation from
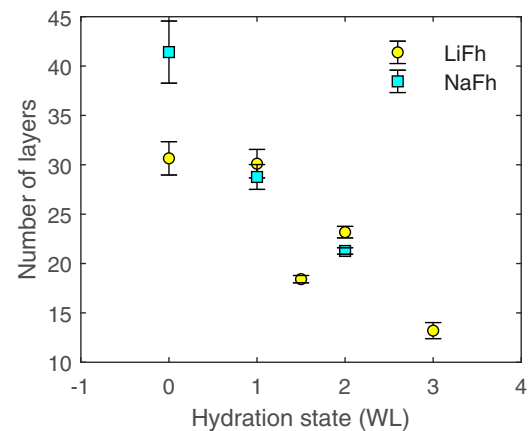

FIG. 10. Average number of clay layers within a clay grain, as a function of the hydration state. Both LiFh and NaFh particle sizes decrease as the RH progresses along the capillary length. The error bars denote the statistical uncertainty on the fit to the Scherrer equation.

Refs. [25,60–62] of values for the diffusion coefficients of water in the nanopores of montmorillonite clays under three hydration states (1 WL, 2 WL, and 3 WL) is given in Table I.

For comparison, the diffusion coefficient of water vapor in air has been reported between 2.0×10^{-5} and 2.5×10^{-4} m^2/s at 20 to 21 °C and under relative humidities of 48% and 62% [63].

APPENDIX B: DEPENDENCE OF THE CLAY PARTICLE THICKNESS ON THE HYDRATION STATE

In Fig. 10 we show the dependence of the clay particles' thickness on the hydration state, computed from Scherrer's equation [64]: for NaFh the number of clay planes are approximately 41 for 0 WL, 28 for 1 WL, and 21 for 2 WL, while LiFh goes from 31 planes at 0 WL to 13 at 3 WL.

[1] J. Bear and A. H.-D. Cheng, *Modeling Groundwater Flow and Contaminant Transport* (Springer Science & Business Media, New York, 2010), Vol. 23 .

[2] T. Le Borgne, M. Dentz, P. Davy, D. Bolster, J. Carrera, J.-R. de Dreuzy, and O. Bour, Phys. Rev. E **84**, 015301 (2011).

[3] A. Raoof and S. Hassanizadeh, Water Resour. Res. **49**, 1943 (2013).

[4] J. Jiménez-Martínez, P. d. Anna, H. Tabuteau, R. Turuban, T. L. Borgne, and Y. Méheust, Geophys. Res. Lett. **42**, 5316 (2015).

[5] J. Jiménez-Martínez, T. Le Borgne, H. Tabuteau, and Y. Méheust, Water Resour. Res. **53**, 1457 (2017).

[6] M. W. Becker and A. M. Shapiro, Water Resour. Res. **36**, 1677 (2000).

[7] R. Haggerty, S. W. Fleming, L. C. Meigs, and S. A. McKenna, Water Resour. Res. **37**, 1129 (2001).

[8] B. Berkowitz, S. Emmanuel, and H. Scher, Water Resour. Res. **44**, W03402 (2008).

[9] R. Schumer, M. M. Meerschaert, and B. Baeumer, J. Geophys. Res.: Earth Surface **114**, F00A07 (2009).

[10] R. Haggerty, S. A. McKenna, and L. C. Meigs, Water Resour. Res. **36**, 3467 (2000).

[11] R. Schumer, D. A. Benson, M. M. Meerschaert, and B. Baeumer, Water Resour. Res. **39**, 1296 (2003).

[12] B. Berkowitz, A. Cortis, M. Dentz, and H. Scher, Rev. Geophys. **44**, RG2003 (2006).

[13] C. M. Gramling, C. F. Harvey, and L. C. Meigs, Environ. Sci. Technol. **36**, 2508 (2002).

[14] P. de Anna, J. Jimenez-Martinez, H. Tabuteau, R. Turuban, T. Le Borgne, M. Derrien, and M. Y., Environ. Sci. Technol. **48**, 508 (2014).

[15] S. Guggenheim and R. Martin, Clay. Clay Miner. **43**, 255 (1995).

[16] I. Bihannic, L. J. Michot, B. S. Lartiges, D. Vantelon, J. Labille, F. Thomas, J. Susini, M. Salomé, and B. Fayard, Langmuir **17**, 4144 (2001).

[17] C. Harvey and G. Lagaly, *Developments in Clay Science* (Elsevier, Amsterdam, 2013), Vol. 5, pp. 451–490.

[18] R. P. Tenório, M. Engelsberg, J. O. Fossum, and G. J. da Silva, Langmuir **26**, 9703 (2010).

[19] E. L. Hansen, H. Hemmen, D. d. M. Fonseca, C. Coutant, K. Knudsen, T. Plivelic, D. Bonn, and J. O. Fossum, Sci. Rep. - UK **2**, 618 (2012).

[20] B. Dazas, B. Lanson, A. Delville, J.-L. Robert, S. Komarneni, L. J. Michot, and E. Ferrage, J. Phys. Chem. C **119**, 4158 (2015).

[21] W. P. Gates, L. P. Aldridge, G. Carnero-Guzman, R. A. Mole, D. Yu, G. N. Iles, A. Klapproth, and H. N. Bordallo, Appl. Clay Sci. **147**, 97 (2017).

[22] H. Hemmen, E. G. Rolseth, D. M. Fonseca, E. L. Hansen, J. O. Fossum, and T. S. Plivelic, Langmuir **28**, 1678 (2012).

[23] P. Giesting, S. Guggenheim, A. F. Koster van Groos, and A. Busch, Environ. Sci. Technol. **46**, 5623 (2012).

[24] L. Michels, J. O. Fossum, Z. Rozynek, H. Hemmen, K. Rustenberg, P. A. Sobas, G. N. Kalantzopoulos, K. D. Knudsen, M. Janek, T. S. Plivelic *et al.*, Sci. Rep. - UK **5**, 8775 (2015).

[25] H. N. Bordallo, L. P. Aldridge, G. J. Churchman, W. P. Gates, M. T. Telling, K. Kiefer, P. Fouquet, T. Seydel, and S. A. Kimber, J. Phys. Chem. C **112**, 13982 (2008).

[26] N. Skipper, A. Soper, and M. Smalley, J. Phys. Chem. **98**, 942 (1994).

[27] G. J. da Silva, J. O. Fossum, E. DiMasi, K. J. Måløy, and S. B. Lutnæs, Phys. Rev. E **66**, 011303 (2002).

[28] G. J. da Silva, J. O. Fossum, E. DiMasi, and K. J. Måløy, Phys. Rev. B **67**, 094114 (2003).

[29] L. Michels, L. Ribeiro, M. S. P. Mundim, M. H. Sousa, R. Droppa Jr., J. O. Fossum, G. J. da Silva, and K. C. Mundim, Appl. Clay Sci. **96**, 60 (2014).

[30] G. Grassi, L. Michels, Z. Rozynek, M. Altoé, E. dos Santos, C. da Fonseca, R. Droppa, A. Gholamipour-Shirazi, J. Fossum, and G. da Silva, Eur. Phys. J. Spec. Top. **223**, 1883 (2014).

[31] B. Dazas, B. Lanson, J. Breu, J.-L. Robert, M. Pelletier, and E. Ferrage, Micropor. Mesopor. Mat. **181**, 233 (2013).

[32] R. P. Tenório, L. R. Alme, M. Engelsberg, J. O. Fossum, and F. Hallwass, J. Phys. Chem. C **112**, 575 (2008).

[33] M. A. S. Altoé, L. Michels, E. dos Santos, R. Droppa Jr., G. Grassi, L. Ribeiro, K. Knudsen, H. N. Bordallo, J. O. Fossum, and G. J. da Silva, Appl. Clay Sci. **123**, 83 (2016).

[34] E. C. Donaldson, T. F. Yen, and G. V. Chilingarian, *Developments in Petroleum Science* (Elsevier, Amsterdam, 1989), Vol. 17, pp. 495–510.

[35] R. Pusch, Clay Miner. **27**, 353 (1992).

[36] I. Cousin, P. Porion, P. Renault, and P. Levitz, Eur. J. Soil Sci. **50**, 249 (1999).

[37] G. Løvoll, B. Sandnes, Y. Méheust, K. Måløy, J. Fossum, G. Da Silva, M. Mundim, R. Droppa Jr., and D. d. M. Fonseca, Physica B **370**, 90 (2005).

[38] Y. Méheust, B. Sandnes, G. Løvoll, K. Måløy, J. Fossum, G. da Silva, M. Mundim, R. Droppa, and D. Fonseca, Clay Sci. **12**, 66 (2006).

[39] H. Hemmen, L. R. Alme, J. O. Fossum, and Y. Méheust, Phys. Rev. E **82**, 036315 (2010).

[40] H. Hemmen, L. R. Alme, J. O. Fossum, and Y. Méheust, Phys. Rev. E **83**, 019901(E) (2011).

[41] L. E. Michels, H. Hemmen, R. J. Droppa, G. Grassi, J. G. da Silva, and J. O. Fossum, in *Proceedings of the 2nd International Workshop on Complex Physical Phenomena in Materials, Hotel*

Armação, Porto de Galinhas - PE, Brazil, edited by J. O. Fossum and G. L. Vasconcelos (complexphysics.org, 2012).

[42] J. Crank *et al.*, *The Mathematics of Diffusion* (Oxford University Press, Oxford, 1979).

[43] L. C. Malacarne, R. S. Mendes, I. T. Pedron, and E. K. Lenzi, Phys. Rev. E **63**, 030101 (2001).

[44] D. Gerasimov, V. Kondratieva, and O. Sinkevich, Physica D **239**, 1593 (2010).

[45] R. Metzler and J. Klafter, Phys. Rep. **339**, 1 (2000).

[46] I. Sokolov and J. Klafter, Chaos **15**, 026103 (2005).

[47] E. N. de Azevedo, P. L. de Sousa, R. E. de Souza, M. Engelsberg, M. d. N. d. N. Miranda, and M. A. Silva, Phys. Rev. E **73**, 011204 (2006).

[48] E. N. de Azevedo, L. R. Alme, M. Engelsberg, J. O. Fossum, and P. Dommersnes, Phys. Rev. E **78**, 066317 (2008).

[49] E. L. Cussler, *Diffusion: Mass Transfer in Fluid Systems* (Cambridge University Press, Cambridge, UK, 2009).

[50] K. Knudsen, J. Fossum, G. Helgesen, and M. Haakestad, Physica B **352**, 247 (2004).

[51] K. D. Knudsen, J. O. Fossum, G. Helgesen, and V. Bergaplass, J. Appl. Crystallogr. **36**, 587 (2003).

[52] F. Salles, O. Bildstein, J. Douillard, M. Jullien, J. Raynal, and H. Van Damme, Langmuir **26**, 5028 (2010).

[53] P. Straka and S. Fedotov, J. Theor. Biol. **366**, 71 (2015).

[54] I. Krasnov, T. Seydel, and M. Müller, Phys. Rev. E **91**, 042716 (2015).

[55] R. Metzler, W. G. Glöckle, and T. F. Nonnenmacher, Physica A **211**, 13 (1994).

[56] H. Z. Cummins, J. Noncryst. Solids **353**, 3891 (2007).

[57] A. Neaman, M. Pelletier, and F. Villieras, Appl. Clay Sci. **22**, 153 (2003).

[58] T. J. Tambach, P. G. Bolhuis, E. J. Hensen, and B. Smit, Langmuir **22**, 1223 (2006).

[59] S. Blackband and P. Mansfield, J. Phys. C **19**, L49 (1986).

[60] V. Marry, P. Turq, T. Cartailler, and D. Levesque, J. Chem. Phys. **117**, 3454 (2002).

[61] F.-R. C. Chang, N. Skipper, and G. Sposito, Langmuir **13**, 2074 (1997).

[62] V. Marry and P. Turq, J. Phys. Chem. A **107**, 1832 (2003).

[63] H. Y. Erbil and M. Dogan, Langmuir **16**, 9267 (2000).

[64] P. Scardi, M. Leoni, and R. Delhez, J. Appl. Crystallogr. **37**, 381 (2004).